remote sensing

MDPI

Article

DEM-Based UAV Geolocation of Thermal Hotspots on Complex Terrain

Lucile Rossi *, Frédéric Morandini, Antoine Burglin, Jean Bertrand, Clément Wandon, Aurélien Tollard and Antoine Pieri

Unité Mixte de Recherche Sciences Pour l'Environnement 6134, Université de Corse, CNRS Campus Grimaldi, 20250 Corte, France

* Correspondence: rossi_l@univ-corse.fr

Highlights

What are the main findings?

- A novel DEM-based algorithm is proposed for geolocating thermal hotspots detected by UAVs over both flat and mountainous terrain.
- The method reformulates the Bresenham traversal algorithm into a direction-vector–based approach and introduces a lightweight, cell-level estimation of the optical ray altitude.

What are the implications of the main findings?

- The algorithm enables real-time or post-processed hotspot geolocation with mean positional errors below 4.2 m, even in complex topography.
- Operationally deployed by the Corsican fire services since 2024, the method has already proven effective for field intervention and hotspot monitoring, providing highly valuable operational support.

Abstract

Reliable geolocation of thermal hotspots, such as smoldering embers that can reignite after vegetation fire suppression, deep-seated peat fires, or underground coal seam fires, is critical to prevent fire resurgence, limit prolonged greenhouse gas emissions, and mitigate environmental and health impacts. This study develops and tests an algorithm to estimate the GPS positions of thermal hotspots detected in infrared images acquired by an unmanned aerial vehicle (UAV), designed to operate over flat and mountainous terrain. Its originality lies in a reformulated Bresenham traversal of the digital elevation model (DEM), combined with a lightweight, ray-tracing-inspired strategy that efficiently detects the intersection of the optical ray with the terrain by approximating the ray altitude at the cell level. UAV flight experiments in complex terrain were conducted, with thermal image acquisitions performed at 60 m and 120 m above ground level and simulated hotspots generated using controlled heat sources. The tests were carried out with two thermal cameras: a Zenmuse H20T mounted on a Matrice 300 UAV flown both with and without Real-Time Kinematic (RTK) positioning, and a Matrice 30T UAV without RTK. The implementation supports both real-time and post-processed operation modes. The results demonstrated robust and reliable geolocation performance, with mean positional errors consistently below 4.2 m for all the terrain configurations tested. A successful real-time operation in the test confirmed the suitability of the algorithm for time-critical intervention scenarios. Since July 2024, the post-processed version of the method has been in operational use by the Corsica fire services.

check for updates

Academic Editor: Tomaž Podobnikar

Received: 4 August 2025
Revised: 23 October 2025
Accepted: 25 November 2025
Published: 2 December 2025

Citation: Rossi, L.; Morandini, F.; Burglin, A.; Bertrand, J.; Wandon, C.; Tollard, A.; Pieri, A. DEM-Based UAV Geolocation of Thermal Hotspots on Complex Terrain. *Remote Sens.* **2025**, *17*, 3911. https://doi.org/10.3390/rs17233911

Copyright: © 2025 by the authors. Licensee MDPI, Basel, Switzerland. This article is an open access article distributed under the terms and conditions of the Creative Commons Attribution (CC BY) license (https://creativecommons.org/licenses/by/4.0/).

Keywords: UAV; thermal image; hotspot; geolocation; DEM; reformulated Bresenham traversal; ray-tracing-inspired strategy; real experiments; complex regions

1. Introduction

Wildfires are a major natural hazard worldwide, threatening human lives, infrastructure, and ecosystems and causing severe ecological and economic losses. Each year, they burn more than 340 million hectares of vegetation [1,2]. Climate change is expected to amplify their impacts by increasing the likelihood and intensity of fire events [3–6].

Regions previously considered to be at low risk are now increasingly exposed to wildfires. Countries such as the United Kingdom, Slovenia, Switzerland, Norway and Finland have recently experienced more frequent and severe vegetation fires, driven by prolonged droughts and rising temperatures.

In recent years, several European countries historically unaccustomed to wildfires have experienced a growing number of vegetation fires. In the United Kingdom, 2022 marked a record number of wildfires, largely driven by unprecedented heatwaves and drought conditions [7,8]. Slovenia experienced its largest recorded wildfire in the Karst region, burning more than 3700 hectares, injuring 17 firefighters and forcing the evacuation of several villages [9,10]. In 2023, Switzerland and Norway also faced significant fire events (particularly in the Valais and Flatanger regions) that caused large-scale emergency responses [11–14].

Beyond these emerging fire-prone regions, France experienced one of the most intense wildfire events in July 2022. Two major wildfires in the Gironde department, Landiras 1 and La Teste-de-Buch, burned a combined 20,800 hectares of forest. Although the flames were largely contained within a few days, the smoldering embers persisted for weeks, particularly in peat-rich and lignite-bearing soils.

These underground hotspots, fueled by organic material up to five meters below the surface, maintained temperatures exceeding 200 °C [15]. More than 40 active hotspots were still being monitored several weeks after the main fires, requiring the continuous intervention of more than 300 firefighters and military personnel [16].

Such residual combustion zones represent a critical hazard, as they can re-ignite fires even after surface containment has been achieved. This phenomenon, known as peat fire or underground smoldering combustion, is well documented worldwide.

In 2015, peat fires in Indonesia burned more than 2.6 million hectares and released more than 1.6 gigatons of CO_2 [17]. In Siberia and Canada, these fires contribute disproportionately to total wildfire emissions due to their persistence below the surface [18].

Similar long-lasting and dangerous smoldering processes are observed in coal seam fires. In regions such as Centralia (USA) and Jharia (India), underground coal deposits have been burning for decades, releasing toxic gasses, damaging infrastructure, and forcing displacement of local populations [19,20].

Like peat fires, coal seam fires are sustained by subsurface combustible materials, often in poorly ventilated environments, making them particularly difficult to detect and extinguish. In both cases, residual hotspots can persist in large areas and remain active for extended periods ranging from months to years, requiring significant human and logistical resources for effective monitoring and control.

The detection and monitoring of residual fire zones, whether in surface vegetation, peat layers, or coal seams, are essential to mitigate the risks of re-ignition and long-term environmental damage. In this study, a hotspot is defined as a spatially localized area whose surface temperature markedly exceeds that of the surrounding environment. Such

thermal anomalies may correspond to smoldering embers, peat fires, or underground combustion zones that persist after fire suppression.

Thermal remote sensing, particularly the use of Unmanned Aerial Systems (UASs) equipped with radiometric thermal cameras, has proven to be an effective tool for mapping residual hotspots. In France, UAVs were deployed to detect smoldering areas several weeks after the containment of the Gironde wildfires [21].

Similar applications have been reported worldwide. In the United States, thermal drones have been used to identify hidden hotspots during wildfire response operations [22,23]. In Indonesia, UAVs have successfully detected persistent peat fires within plantation areas [24]. In China, UAV-based thermal imaging has been used to monitor coal seam fires and locate underground combustion zones [25].

In parallel, research has increasingly focused on improving the automation and accuracy of hotspot detection and geolocation, i.e., the process of determining the precise geographic coordinates of hotspots on the Earth's surface using aerial platforms. Various systems have been proposed to process thermal and visual data from UASs for real-time fire monitoring and analysis [26–33]. Since the early 2000s, studies have addressed the challenges of detecting early-stage fires and smoldering embers, collectively referred to as hotspots, through the integration of remote sensing data with onboard navigation systems [34–39].

Wright et al. [40], for example, introduced a system using long-wave infrared (LWIR) imagery and photogrammetric techniques to geolocate ignition points from fire. Although the method incorporated a wide area differential global positioning system (WADGPS) and an Inertial Navigation System for georeferencing, the photogrammetric process remained undocumented and only a limited test campaign was conducted. Graml and Wigley [41] proposed a UAV-based platform that combined visual and thermal sensors to improve ember tracking, but without any reported experimental validation.

More recently, Allison et al. [42] reviewed the state of the art in airborne fire detection systems, highlighting the benefits of thermal infrared imagery (especially in the 8–15 μm range) for its ability to detect heat sources even through thick smoke. Field-oriented efforts have also emerged: Viseras et al. [43] conducted the first structured campaign using commercial drones equipped with the GNSS-RTK (Real-Time kinetic Global Positioning System) to capture thermal and visual data from wildfire hotspots, although without providing quantitative accuracy results. Li et al. [44] combined thermal thresholding and homography-based georeferencing in a UAS experiment, achieving position errors below 1.42 m at low altitude and up to 5.93 m under flat terrain conditions.

The search for a target on the ground with precision in mountainous regions presents a significant challenge. Cai [45] conducted a review of target geolocation algorithms for aerial remote sensing cameras without ground control points.

Six main algorithms are identified: the basic coordinate transformation method, the geolocation algorithm based on the Earth ellipsoid model, the method using a digital elevation model (DEM), the active positioning technique employing a laser range sensor, the triangulation-based approach using single or dual UAV configurations, and the filtering-based method relying on multiple measurements from a single UAV.

Among these, the DEM-based geolocation method is reported to be the most suitable for locating ground targets in mountainous terrain, particularly from images acquired by civil UAVs flying at altitudes up to 150 m. This approach relies on ray tracing [46] combined with the Bresenham algorithm [47], allowing an approximate intersection computation between the optical ray and the DEM of the observed area. The optical ray is defined as a 3D line extending from the camera optical center through the image pixel corresponding to the target, while the DEM represents the terrain as a discrete grid of elevation values.

The Bresenham algorithm, originally developed for raster line rendering [48], is used to traverse the grid cells intersected by the ray and evaluate potential intersection points.

Other studies have adopted similar strategies. For example, in [49], a Bresenham-like traversal algorithm is used to identify the first DEM cell intersected by the optical ray. The vertical projection of the ray onto the DEM is followed, starting from the grid cell directly beneath the UAV. Each cell crossed by the ray is evaluated until the DEM elevation exceeds the corresponding ray height. However, the calculation of the ray altitude along this traversal is only conceptually described in the parametric form $(X_0, Y_0) + k(U, V)$, without providing an explicit formulation to determine the corresponding Z coordinate at each step, which makes the practical implementation and accuracy assessment of intersection detection unclear in complex terrain.

In contrast, the method described by Santana [50] advances directly along the 3D ray in the direction of the target. At each step, it compares the elevation of the ray with the terrain height in the corresponding DEM cell, terminating the traversal when the ray is found to be below the surface. However, this ray-tracing strategy requires iterative sampling along the 3D ray, making its performance strongly dependent on the chosen step size: a coarse discretization may skip the intersection with the terrain, while a fine discretization increases the computational cost and limits its suitability for real-time applications.

Such ray-based methods have also been applied in wildfire mapping applications [29,50,51]. In particular, the method proposed by Santana [50] integrates this approach with an extended Kalman filter based on bearing and range measurements to georeference aerial images of active fire fronts. However, it should be noted that the validation of these methods has been limited to computational simulations, with no field-tested implementation reported to date.

To our knowledge, no existing UAS software solution has been field tested for the geolocation of thermal hotspots across varied terrains, and in particular not in mountainous environments with quantitative assessment using accurate GNSS ground truth. The method proposed in this paper is designed to maintain consistent performance and accuracy of meter-level geolocation in both flat and mountain areas with significant elevation changes. We introduce a dedicated algorithm, implemented on a commercial UAS platform, that combines thermal infrared imagery with a DEM and employs a terrain traversal strategy inspired by the Bresenham algorithm to accurately project thermal detections onto the ground.

This paper is organized as follows: after the introduction, Section 2 describes the proposed method and the hotspot geolocation algorithm based on a reformulated Bresenham traversal and a cell-level estimate of the optical ray altitude. Section 3 presents the experimental setup (test sites, UAV platforms and sensors, flight configurations, DEM data) and how the algorithm is run. Section 4 reports the field results, including geolocation errors, the effect of DEM resolution, processing time, and an operational example from a real wildfire in which the software was used by firefighters. Section 5 discusses the findings and limitations. Section 6 concludes the paper and outlines future work.

The main contribution of this work lies in the DEM-based estimation of hotspot locations, achieved through the computation of the optical ray–terrain intersection. This approach combines a generalized Bresenham traversal with a lightweight altitude estimation model, providing an efficient alternative to full 3D ray tracing while maintaining accuracy on complex terrain. By emphasizing this DEM–thermal image superposition principle, the proposed method directly addresses the operational need for reliable and computationally efficient hotspot geolocation.

2. Method

This section details the method developed to geolocate thermal hotspots specifically designed to operate in complex terrains, including both flat and mountainous environments. The approach integrates the acquisition and processing of infrared imagery captured by a UAV and focuses on computing the GNSS coordinates of the detected hotspots. The proposed method combines a reformulated version of the Bresenham algorithm, adapted to operate from a starting point and a direction vector, with an elevation estimation approach inspired by the principle of ray tracing, where the altitude of the optical ray is computed at each DEM cell along the path. The methodology is described step by step in the following sections.

The methodological description begins with the definition of coordinate frames and associated transformations, which are fundamental to understanding the proposed geolocation method.

2.1. Basic Coordinate Frames and Transformations

In the proposed method, seven coordinate frames are considered (Figure 1): pixel, camera, gimbal, drone, NED world, ENU world, and local ENU.

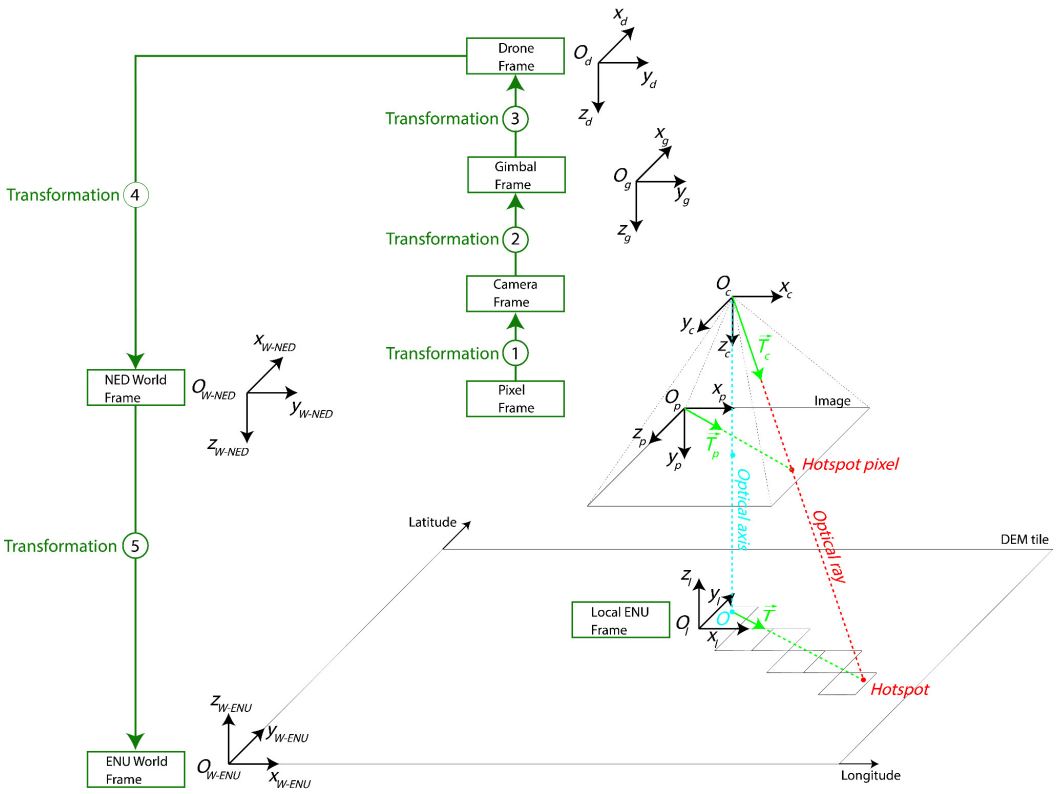

Figure 1. Frames and transformations used in the geolocation process.

These frames follow standard aerospace and photogrammetric conventions. The pixel frame is defined by the image axes, the camera frame by the optical center and axis, the gimbal frame by the stabilized mount, and the drone frame by the UAV body axes. The NED frame corresponds to the UAV attitude reference (yaw, pitch, roll), while the ENU frame is aligned with the DEM. The local ENU frame is anchored at the DEM cell that contains the projection of the camera center and shares the orientation of the global ENU frame. For simplicity, the drone, gimbal, and camera centers are assumed co-located, given that their offsets are negligible relative to the flight altitude. Coordinate transformations follow the ZYX convention. The intrinsic matrix K maps the pixel coordinates to the camera

frame. $R_{G\to C}$ aligns the camera and gimbal frames through fixed rotations. $R_{D\to G}$ applies the gimbal attitude angles (yaw, pitch, and roll). $R_{W_{NED}\to D}$ applies the UAV attitude angles in the NED frame. Finally, $R_{W_{ENU}\to W_{NED}}$ converts between the ENU and NED conventions. The complete rotation from the ENU world to the camera frame is, therefore, expressed as

$$R_{W_{ENU}\to C} = R_{G\to C} \cdot R_{D\to G} \cdot R_{W_{NED}\to D} \cdot R_{W_{ENU}\to W_{NED}} \quad (1)$$

This chain of transformations allows the coordinates of the pixels to be projected into directional vectors expressed in the ENU world frame, which form the geometric basis of the geolocation algorithm described in Section 2.2.

The thermal camera was assumed to be factory calibrated, with intrinsic parameters provided by the manufacturer. Lens distortions were considered negligible at the flight altitudes investigated (60–120 m), where residual pixel-level errors translate to subdecimetric geolocation shifts, well below the targeted meter-level accuracy. The stabilization of the gimbal ensures a nadir pointing, which minimizes boresight offsets between the camera and the UAV body frame.

2.2. Hotspot Geolocation Algorithm

This section describes the geolocation algorithm step by step. The process starts with thermal image acquisition and recording the optical sensor pose, followed by hotspot detection in the image. Each detected hotspot is then individually processed. This involves computing the direction vector of the optical ray, projecting the optical center and direction vector onto the DEM plane, traversing the DEM, and evaluating the intersection with the terrain. A final data grouping and clustering step provides georeferenced hotspot positions for operational use. The detailed procedure is presented in the following subsections.

2.2.1. Step 1—Thermal Image Acquisition

The proposed algorithm is implemented in dedicated software that processes thermal infrared images captured by the drone's on-board camera. It supports both radiometric images, which contain raw temperature data, and isothermal images, where pixel values are mapped to a color palette within a specified temperature range. In the case of isothermal images, a minimum temperature threshold is defined, serving as the detection limit for hotspots, along with a maximum temperature and a color palette selected from those available on the imaging system. This design ensures compatibility with a variety of thermal imaging configurations without relying on specific hardware brands or models. The currently supported color palettes include Fulgurite, Medical, IronRed, and HotIron, among others [52].

2.2.2. Step 2—Optical Sensor Pose Recording

The position and orientation of the optical sensor at the time of image acquisition are extracted from the metadata embedded in each thermal image. These data, expressed in a geographic coordinate system (WGS84 in this study), include the GNSS position and the camera attitude angles (yaw, pitch, and roll). The GNSS coordinates are subsequently converted into the ENU world frame, aligned with the corresponding DEM tile expressed in the Lambert 93 projection, which serves as a reference for the geolocation process.

2.2.3. Step 3—Hotspot Detection and Pixel-Level Extraction

Hotspots are detected and localized in each radiometric or isothermal thermal image, and the corresponding pixel coordinates and temperature values are extracted.

For radiometric images, which provide raw temperature values per pixel, a black-and-white image is created by selecting only the pixels whose temperature exceeds a

user-defined threshold. This binary image is then processed using a median filter to reduce noise, followed by a blob analysis to detect connected regions. Each labeled region is considered a hotspot, and its centroid defines its position in the pixel frame.

For isothermal images, which are generated using a minimum and maximum temperature range and a predefined color palette configured on the imaging system, the hotspot detection is based on identifying the pixels that have been color-mapped, i.e., whose temperature lies within the specified range. Once these pixels are identified, the same processing steps as with radiometric images are applied: binarization, filtering, and blob analysis. Each hotspot is then localized using the centroid of its corresponding region.

In both cases, the representative temperature of each detected hotspot is defined as the maximum temperature among the pixels that belong to the corresponding region.

2.2.4. Step 4—Per-Hotspot Processing

The following sub-steps are repeated for each hotspot detected in the thermal image.

Step 4.1—Computation of the direction vector in the camera frame

Starting from the homogeneous pixel vector $\vec{T}_p = (u, v, 1)^\top$ of the centroid hotspot in the image, this vector is transformed into the camera frame by applying the intrinsic inverse matrix:

$$\vec{T}_c = K^{-1} \cdot \vec{T}_p \tag{2}$$

which gives the direction of the optical ray from the optical center of the camera through the hotspot in the camera coordinate system.

Step 4.2—Projection of the optical center and Direction Vector in the DEM Plane (in the ENU frame)

The optical center $\mathcal{O}_c$ is orthogonally projected onto the horizontal plane corresponding to the DEM surface, resulting in the point $\mathcal{O}$ within the local ENU coordinate system, which shares its orientation with the global ENU frame but is anchored at the reference point of the DEM grid cell that contains the projection of $\mathcal{O}_c$.

The direction vector $\vec{T}_c$ obtained in Step 4.1 is expressed in the global ENU coordinate system by applying the transpose of the complete rotation matrix:

$$\vec{T} = R^\top_{W_{ENU} \to C} \cdot \vec{T}_c \tag{3}$$

which gives the directional vector $\vec{T}$ pointing toward the hotspot in the ENU reference frame.

This vector $\vec{T}$, expressed in the ENU coordinate system, is projected onto the horizontal plane of the DEM by retaining only its x and y components, thus defining a 2D direction vector used to traverse the DEM grid cells starting from the projected optical center $\mathcal{O}$.

Step 4.3—DEM Traversal Along the Projected Direction

A DEM is a raster data set that represents the elevation of the terrain through a grid of discrete cells arranged in rows and columns. Each cell covers a surface area of size $r_x \times r_y$, where r_x and r_y denote the spatial resolutions in the east–west and north–south directions, respectively. Each cell stores an elevation value relative to a defined vertical reference system, such as the mean sea level or an ellipsoidal height.

Starting from the cell containing $\mathcal{O}$, the DEM is traversed along the direction vector $\vec{T}$, using the Bresenham algorithm [47], reformulated to operate from a given starting point and a specified direction vector.

The original Bresenham algorithm was designed to determine the sequence of discrete cells that form a straight line between a specified starting cell and an ending cell. However, in the context of this study, the location of the hotspot is unknown, making it impossible to

define the endpoint required by the original Bresenham algorithm. Therefore, the algorithm has been reformulated to take as input a starting point and a direction vector, with the traversal beginning in the cell containing $\mathcal{O}$ and proceeding along $\vec{T} = (dx, dy)$.

Consider the $x_l y_l$ plane defined by the x_l and y_l axes of the local ENU frame $\mathcal{F}_L$, with origin $\mathcal{O}_l$ and axes (x_l, y_l, z_l). This frame is anchored at the reference point of the DEM cell containing the projected camera center $\mathcal{O}$, shares the same orientation as the global ENU world frame, and provides a convenient basis for 2D traversal over the DEM grid.

This $x_l y_l$ plane can be divided into eight octants based on the signs of dx and dy, and on the relative magnitudes of $|dx|$ and $|dy|$. Each octant corresponds to a unique combination of these values and reflects the predominant direction of $\vec{T}$, as illustrated in Figure 2.

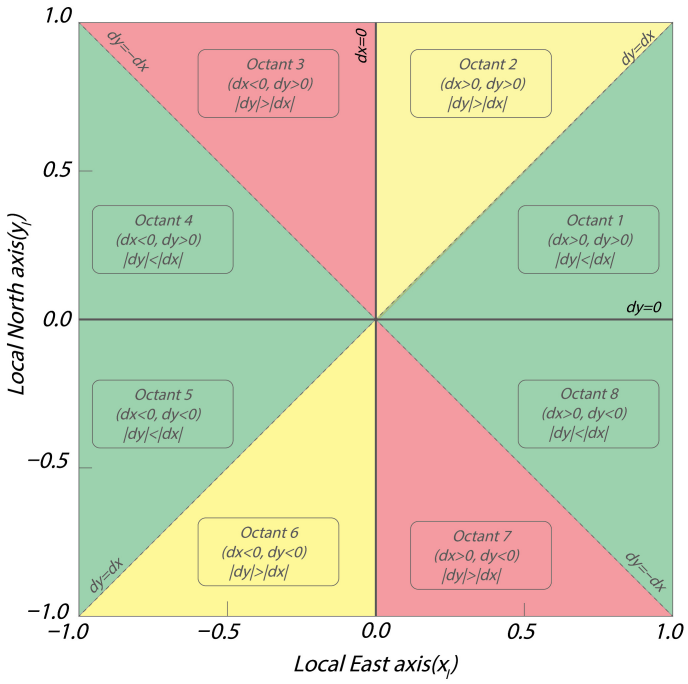

Figure 2. Division of the $x_l y_l$ plane into octants based on the components of $\vec{T}$. Octants shaded in green satisfy $|dy| < |dx|$. Octants shaded in yellow satisfy $|dy| > |dx|$ with $\text{sign}(dx) = \text{sign}(dy)$. Octants shaded in red satisfy $|dy| > |dx|$ with $\text{sign}(dx) \neq \text{sign}(dy)$.

In octants 1, 4, 5 and 8, where $|dy| < |dx|$, progression occurs primarily along the x_l axis, with occasional steps along y_l. When $dy = 0$, the trajectory is strictly aligned with the x_l axis.

In octants 2, 3, 6 and 7, where $|dy| > |dx|$, progression occurs primarily along y_l, with occasional steps along x_l. When $dx = 0$, the trajectory follows the y_l axis exclusively.

Along the diagonals $dx = dy$ and $dx = -dy$, the motion is equally distributed across both axes, producing diagonal trajectories at 45° and 135°, respectively.

The traversal strategy is initially presented in the first octant and then generalized to all directions.

Let (x, y) denote the coordinates of the current DEM cell, and let $\vec{T} = (dx, dy)$ be a direction vector in the first octant such that $dx > 0$, $dy > 0$, and $|dy| < |dx|$. The algorithm iteratively proceeds from the initial cell in the direction of $\vec{T}$, guided by the decision variable ζ, initially set to $\zeta = 2 \cdot dy - dx$, as originally proposed by Bresenham [47]. At each iteration, ζ determines whether the next cell is chosen horizontally or diagonally, to minimize the deviation from the ideal continuous line defined by $\vec{T}$. Figure 3 illustrates the cell-to-cell transition driven by ζ.

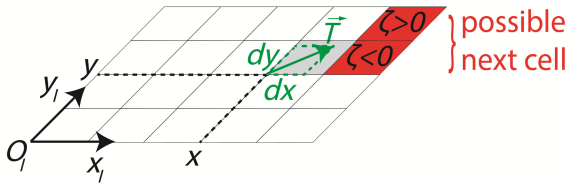

Figure 3. Cell-to-cell transition mechanism governed by the variable ζ during the discrete traversal of the DEM.

The following steps are repeated iteratively:

1. A unit increment is performed along the x_l axis;
2. The variable ζ is evaluated:
   - If $\zeta < 0$, the same row y_l is maintained.
     Update: $\zeta \leftarrow \zeta + 2 \cdot dy$;
   - Otherwise, a unit step is also performed along y_l.
     Update: $\zeta \leftarrow \zeta + 2 \cdot (dy - dx)$.

This process is detailed in Algorithm 1, where `iter_max` ensures finite execution.

Algorithm 1 Bresenham algorithm in the first octant with a starting point and a direction vector

Require: Current cell (x, y), direction vector $\vec{T} = (dx, dy)$ with $dx > 0$, $dy > 0$, and $|dy| < |dx|$; maximum number of steps `iter_max`
Ensure: Cells to be successively considered

```
ζ ← 2 · dy − dx
for i from 0 to iter_max do
    x ← x + 1
    if ζ < 0 then
        ζ ← ζ + 2 · dy
    else
        y ← y + 1
        ζ ← ζ + 2 · (dy − dx)
    end if
end for
```

To extend the algorithm to all eight octants of the $x_l y_l$ plane, its core logic is preserved but adapted to directional variations. The direction of propagation is determined by the signs of dx and dy, and the dominant traversal axis by comparison between $|dx|$ and $|dy|$.

When $|dx| > |dy|$, the algorithm progresses primarily along x_l, with conditional changes in y_l.

When $|dy| > |dx|$, the axes are swapped and the traversal proceeds along y_l, requiring a coordinate transformation (offset).

Case 1—Same sign ($\text{sign}(dx) = \text{sign}(dy)$; octants 2 and 6).

$$\begin{aligned} \text{The offset is defined as:} \quad & \mathit{offset} = \text{sign}(dx) \cdot x - \text{sign}(dy) \cdot y, \\ \text{and the corrected coordinates are:} \quad & x_{\text{corr}} = y + \text{sign}(dy) \cdot \mathit{offset}, \\ & y_{\text{corr}} = x - \text{sign}(dx) \cdot \mathit{offset}. \end{aligned}$$

Case 2—Opposite sign ($\text{sign}(dx) \neq \text{sign}(dy)$; octants 3 and 7).

$$\begin{aligned} \text{The offset is defined as:} \quad & \mathit{offset} = \text{sign}(dx) \cdot x + \text{sign}(dy) \cdot y, \\ \text{and the corrected coordinates are:} \quad & x_{\text{corr}} = y - \text{sign}(dy) \cdot \mathit{offset}, \\ & y_{\text{corr}} = x - \text{sign}(dx) \cdot \mathit{offset}. \end{aligned}$$

These transformations allow the algorithm to operate uniformly in a consistent reference frame, regardless of the original orientation of $\vec{T}$. After each step, the corrected coordinates are mapped back to the original frame, ensuring continuity across the octants and DEM tiles.

Algorithm 2 summarizes the generalized Bresenham algorithm adapted to all octants.

Algorithm 2 Generalized Bresenham algorithm for all octants using a starting point and a direction vector

Require: Starting point (x, y), direction vector $\vec{T} = (dx, dy)$, number of iterations `iter_max`
Ensure: Cells to be successively considered

$sx \leftarrow \text{sign}(dx)$
$sy \leftarrow \text{sign}(dy)$
$dx \leftarrow |dx|, dy \leftarrow |dy|$
if $dx = 0$ **then**
  for $i = 0$ to `iter_max` **do**
    $y \leftarrow y + sy$
  end for
else if $dy = 0$ **then**
  for $i = 0$ to `iter_max` **do**
    $x \leftarrow x + sx$
  end for
else if $dx = dy$ **then**
  for $i = 0$ to `iter_max` **do**
    $x \leftarrow x + sx$
    $y \leftarrow y + sy$
  end for
else if $dx > dy$ **then**
  $\zeta \leftarrow 2 \cdot dy - dx$
  for $i = 0$ to `iter_max` **do**
    $x \leftarrow x + sx$
    if $\zeta < 0$ **then**
      $\zeta \leftarrow \zeta + 2 \cdot dy$
    else
      $y \leftarrow y + sy$
      $\zeta \leftarrow \zeta + 2 \cdot (dy - dx)$
    end if
  end for
else
  if $\text{sign}(dx) = \text{sign}(dy)$ **then**
    $offset \leftarrow sx \cdot x - sy \cdot y$
    $x \leftarrow y + sy \cdot offset$
    $y \leftarrow x - sx \cdot offset$
  else
    $offset \leftarrow sx \cdot x + sy \cdot y$
    $x \leftarrow y - sy \cdot offset$
    $y \leftarrow x - sx \cdot offset$
  end if
  $\zeta \leftarrow 2 \cdot dx - dy$
  for $i = 0$ to `iter_max` **do**
    $y \leftarrow y + sy$
    if $\zeta < 0$ **then**
      $\zeta \leftarrow \zeta + 2 \cdot dx$
    else
      $x \leftarrow x + sx$
      $\zeta \leftarrow \zeta + 2 \cdot (dx - dy)$
    end if
  end for
end if

Step 4.4—Evaluation of Optical Ray–Terrain Intersection

During DEM traversal, the algorithm estimates the elevation of the optical ray at the position (x, y) of each DEM cell visited to determine whether the ray intersects the surface of the terrain at that location. Rather than computing the full 3D trajectory of the ray, a geometric approximation is adopted as detailed below. This approach significantly reduces computational complexity while providing sufficient accuracy for detecting intersections in real-time or near-real-time processing.

The geometric configuration is illustrated in Figure 4. The optical center of the camera, $O_c = (0, 0, h_{oc})$, is expressed in the local ENU frame, and its orthogonal projection into the $x_l y_l$ plane (corresponding to the DEM plane) is O. The DEM cell containing O defines the starting cell of the traversal and anchors the local ENU reference frame $\mathcal{F}_L$, whose origin $\mathcal{O}_l$ is set at the bottom-left corner of this cell. The optical ray is defined by the unit direction vector $\vec{T}_c = (T_{c_x}, T_{c_y}, T_{c_z})$, while the optical axis of the camera is aligned with $\vec{N} = (0, 0, 1)$.

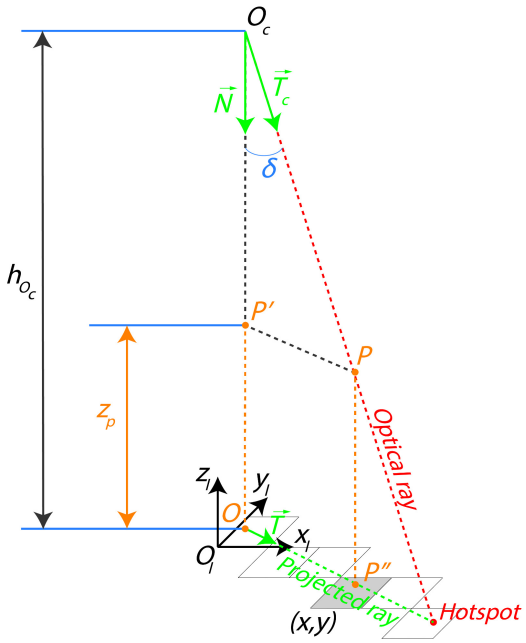

Figure 4. Geometric configuration for estimating the optical ray elevation at a DEM cell.

Let P be a point on the optical ray. Its orthogonal projection onto the DEM plane is P'', and its projection onto the segment $\overline{OO_c}$ is P', forming a right triangle (P, P', O_c) with a right angle at P'. The point P is chosen so that P'' lies within the current DEM cell traversed by the projected optical ray.

Step 4.4.1 Estimation of the Optical Ray Altitude within a DEM Cell

Based on the geometric setup previously described, the estimated altitude of the optical ray at position P, denoted z_P, is given by the vertical distance between P and the DEM plane, corresponding to the segment $P''P = OP'$. It is calculated by subtracting the length $\|O_c P'\|$ from the known height of the camera above the DEM plane, $\|O_c O\| = h_{oc}$, as follows:

$$OP' = h_{oc} - \|O_c P'\| \tag{4}$$

The length $\|O_c P'\|$ is calculated from the right triangle (P, P', O_c) using the incidence angle δ, defined as the angle between the unit direction vector of the optical ray $\vec{T}_c$ and the unit direction vector of the optical axis of the camera $\vec{N} = (0, 0, 1)$. Angle δ is computed via the dot product:

$$\begin{aligned}\langle \vec{T}_c, \vec{N} \rangle &= T_{c_x} N_x + T_{c_y} N_y + T_{c_z} N_z \\ &= \cos(\delta) = T_{c_z}\end{aligned} \tag{5}$$

which gives

$$\delta = \arccos(T_{c_z}) \tag{6}$$

From the same triangle, one has

$$\tan(\delta) = \frac{\|PP'\|}{\|O_c P'\|} \tag{7}$$

solving for $\|O_c P'\|$ gives

$$\|O_c P'\| = \frac{\|PP'\|}{\tan(\delta)} \tag{8}$$

Geometrically, the horizontal distance between P and P' is equal to the horizontal distance between O and P'' in the configuration described above, i.e., $\|PP'\| = \|OP''\|$. The current cell is indexed by its discrete coordinates (x, y) in the DEM grid, and the DEM resolutions along the x and y directions are denoted r_x and r_y, respectively. The horizontal distance $\|OP''\|$ is approximated by $d_{x,y}$, defined as the Euclidean distance from the bottom left corner of the current DEM cell to the origin O_L of the local ENU frame. Figure 5 illustrates two examples of the distance d_{x_i,y_i}, calculated between the origin O_L of the local ENU frame and the projection P'' of a point P located on the optical ray, where P'' lies within the DEM cell indexed by (x_i, y_i). In the figure, the distances d_1 and d_3 correspond to the cells (x_1, y_1) and (x_3, y_3), respectively. The metric coordinates of the current cell are then given by $(x_m, y_m) = (x \cdot r_x, y \cdot r_y)$, and the resulting approximation reads

$$d_{x,y} = \sqrt{(x \cdot r_x)^2 + (y \cdot r_y)^2} \tag{9}$$

Combining Equations (4), (6), (8) and (9), the estimated height of the optical ray at the point P can be expressed as

$$z_P = h_{oc} - \frac{d_{x,y}}{\tan(\delta)} = h_{oc} - \frac{\sqrt{(x \cdot r_x)^2 + (y \cdot r_y)^2}}{\tan(\arccos(T_{c_z}))} \tag{10}$$

This approximation assumes that all ray points whose projections fall within the same DEM cell share the same elevation estimate, which is a reasonable simplification for efficient processing. Furthermore, experimental validations have shown that using the orthogonal projection of the drone position on the DEM plane (point O) or the origin of the local ENU frame as the reference for computing the horizontal distance $d_{x,y}$ leads to negligible differences in the estimates of heights resulting. This supports the robustness of the proposed model in practical implementations, regardless of the specific reference point used within the DEM grid.

Finally, the estimated elevation z_P of the ray is compared to the elevation of the DEM in the corresponding cell. If the elevation of the terrain is greater than z_P, the intersection is considered to occur within this cell and the traverse is terminated. This test constitutes the intersection detection step and the hotspot is then assigned the GNSS position of the corresponding DEM cell.

The following subsections further detail the treatment of potential errors inherent in the geometric approximation, including the derivation of a maximum error bound and the definition of an exclusion zone in the image plane where the altitude estimation is considered unreliable.

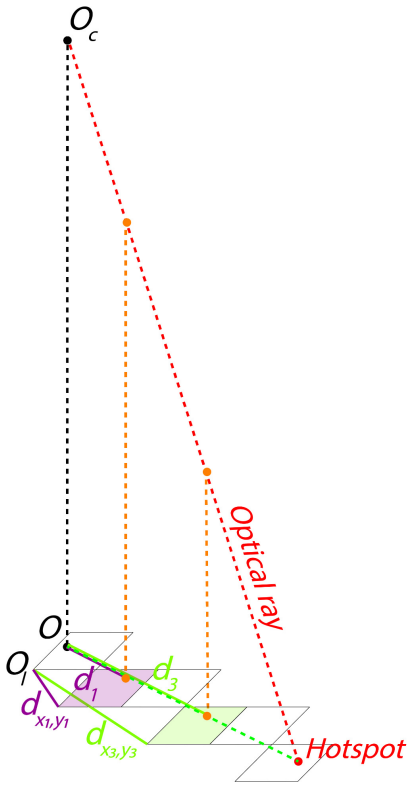

Figure 5. Geometric approximation of the horizontal distance $d_{x,y}$ from the current DEM cell to the local ENU origin O_L.

Step 4.4.2 Maximum Error Bound and Exclusion Zone

Maximum error bound.The geometric approximation introduced above assumes that the optical ray altitude can be estimated from a reference distance $d_{x,y}$ calculated within the local ENU grid. However, the actual intersection between the optical ray and the terrain may occur at a different horizontal location within the cell, resulting in a potential horizontal offset Δd relative to the assumed reference distance.

This horizontal offset leads to a vertical error in the altitude estimation of the ray. This vertical error ε_z can be bounded using the geometric relation that links the horizontal offset Δd to the altitude error:

$$\varepsilon_z = \left| \frac{\Delta d}{\tan(\delta)} \right| \tag{11}$$

In practice, a conservative upper bound on the vertical error is obtained by substituting the maximum possible horizontal deviation $d_{\max}$, corresponding to the half diagonal of a DEM cell:

$$d_{\max} = \frac{\sqrt{r_x^2 + r_y^2}}{2} \tag{12}$$

where r_x and r_y denote the DEM resolutions along the x- and y-axes of the ENU grid, respectively.

For a DEM with $r_x = r_y = 1$ m, the maximum possible horizontal deviation becomes

$$d_{\max} = \frac{\sqrt{1^2 + 1^2}}{2} = \frac{\sqrt{2}}{2} \approx 0.71 \text{ m} \tag{13}$$

The resulting maximum vertical error is then expressed as

$$\varepsilon_{z,\max} = \frac{d_{\max}}{\tan(\delta)} \tag{14}$$

As the angle of incidence δ decreases, the error increases dramatically due to the singularity of $\tan(\delta)$ near zero. To mitigate the error induced by this singularity, a minimum threshold $\delta_{\min} = 6^\circ$ is adopted. This value is chosen based on the analytical evolution given in Equation (14), so that the vertical error does not exceed 6.8 m. Figure 6 illustrates the evolution of this error as a function of the angle of incidence.

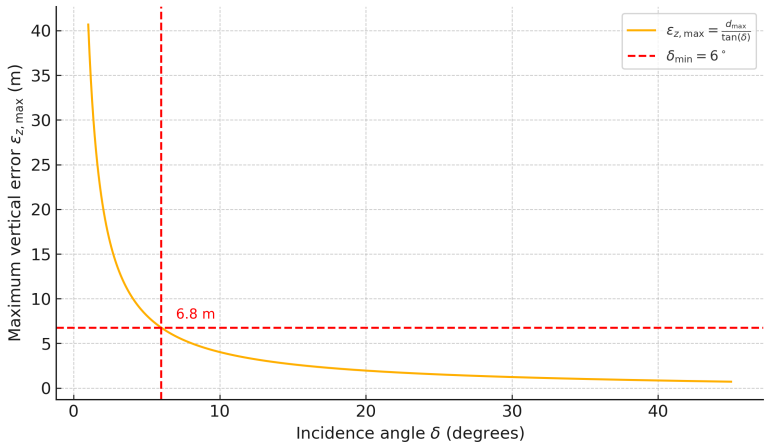

Figure 6. Analytical evolution of the maximum vertical error $\varepsilon_{z,\max} = d_{\max}/\tan(\delta)$ as a function of the incidence angle δ, assuming $d_{\max} = 0.71$ m (i.e., half-diagonal of a 1 m DEM cell).

Definition of the exclude zone in the image plane. The condition $\delta < \delta_{\min}$ defines an exclusion zone in the image where the altitude estimation becomes unreliable. In the pinhole projection model, this region corresponds to an ellipse centered on the principal point (C_x, C_y).

The parameters f_x and f_y represent the focal lengths in pixels along the horizontal and vertical image axes. They are calculated from the physical focal length f, the sensor dimensions (W, H), and the image resolution (N_x, N_y) as

$$f_x = \frac{f \cdot N_x}{W}, \quad f_y = \frac{f \cdot N_y}{H} \tag{15}$$

The pixels (u, v) inside this exclusion zone satisfy the inequality

$$\left(\frac{u - C_x}{a}\right)^2 + \left(\frac{v - C_y}{b}\right)^2 < 1 \tag{16}$$

where the ellipse semiaxes are

$$a = f_x \cdot \tan(\delta_{\min}), \quad b = f_y \cdot \tan(\delta_{\min}) \tag{17}$$

Pixels inside this ellipse are excluded from the DEM traversal. The corresponding hotspots are assigned the location of the DEM cell that contains the projection of the optical center O_c, which ensures a bounded error in the nadir region.

An orthophoto-based workflow could also be envisaged for hotspot detection and geolocation. However, orthophoto generation requires high image overlap and substantial computational resources, and infrared imagery is generally less reliable for photogrammetric processing due to its lower spatial resolution and texture. In addition, steep terrain may exacerbate alignment errors and geometric distortions. For these reasons, the ray-tracing workflow was considered more appropriate to ensure both accuracy and operational efficiency in this study.

Step 5—Clustering of Geolocated Hotspots and Temperature Aggregation

After geolocating all selected points in the infrared images, a post-processing step is applied to group nearby points into spatial clusters. This clustering accounts for the fact that multiple geolocated points may correspond to the same physical hotspot, as the latter can be detected in multiple thermal images during the UAV flight. Due to measurement noise and GNSS inaccuracies, the geolocated points associated with a given hotspot do not exactly coincide but instead form a spatially dispersed set of points around the true position.

The clustering threshold is defined as

$$d_{\text{threshold}} = 9 + \max(r_x, r_y) \tag{18}$$

The constant term of 9 m was empirically determined from repeated acquisitions of the same hotspot under varying drone–target distances, flight altitudes, and viewing geometries, with the camera maintained in a nadir orientation. Then a sensitivity analysis was performed on data sets acquired at 60 m (12 clusters, 89 points) and 120 m (18 clusters, 119 points). In both cases, more than 70% of the nearest-neighbor distances were <2 m and approximately 92% were <3 m, confirming compact clusters (Figure 7). A single exceptional case at 120 m exhibited a separation of 8–9 m (≈0.8% of the data set), indicating that smaller thresholds (e.g., 3 m) would fragment individual hotspots.

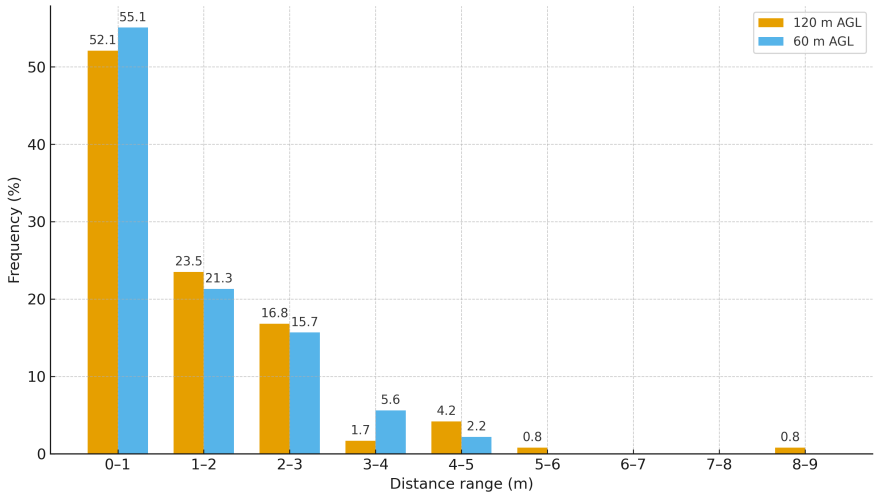

Figure 7. Nearest-neighbor distance distributions at 60 m and 120 m AGL.

For each identified cluster, the centroid position, the maximum observed temperature, and the spatial radius are computed. The spatial radius is defined as the maximum distance between the centroid and any point in the cluster; if all points in the cluster coincide with the centroid position, the radius is set by default to the maximum dimension of a single DEM cell. Together, the centroid and its associated radius define a high-probability zone of hotspot presence, referred to as a search zone in the operational context, which reflects both the estimated position and the spatial dispersion of the observations and represents the region where a hotspot is most likely located. When two or more hotspots are in close proximity, the centroid and radius do not necessarily correspond to a single physical hotspot but rather to a zone of high probability encompassing multiple hotspots.

Step 6—Results Export

Geolocation results are exported in structured formats such as CSV, GeoJSON, or KML. These results can be integrated into external wildfire response and monitoring systems.

3. Experiment

A field campaign was conducted to evaluate the performance of the proposed hotspot geolocation algorithm under realistic conditions, reflecting the complexity of terrains commonly encountered in Corsica. Two sites with contrasting terrain configurations and characteristic Mediterranean maquis vegetation were selected as test areas.

3.1. Test Sites

The two sites, located in different parts of Corsica (France), are Porto-Vecchio (latitude 41.599506, longitude 9.209710) and Soveria (latitude 42.346899, longitude 9.143678), as shown in Figure 8a. They feature contrasting terrain configurations while sharing typical maquis vegetation, including *Pinus pinaster* (maritime pine), *Cistus* (rockrose), *Erica* (heather), and *Arbutus unedo* (strawberry tree).

At the Porto-Vecchio site, a relatively flat area, the surveyed zone measured approximately 90 m × 120 m. The experiment was conducted there on 14 November 2024, under cool ambient conditions.

In contrast, the Soveria site is located in a mountainous region and similar maquis vegetation, as illustrated in Figure 8b. At this site, the surveyed area covered approximately 370 m × 240 m. The experiment was carried out on 28 May 2025, under warmer ambient conditions.

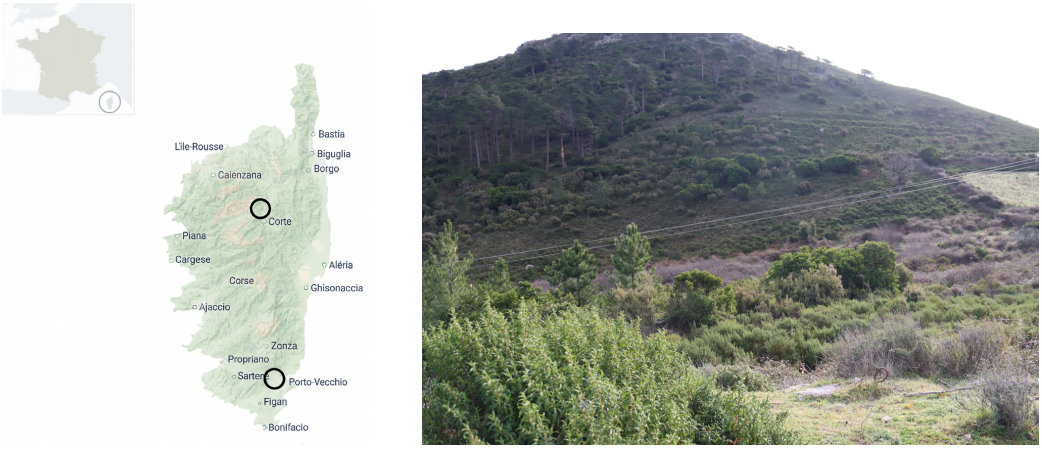

(**a**) Locations in Corsica (**b**) Soveria site terrain and vegetation

Figure 8. Overview of the test sites.

The following subsection describes the aerial platforms, sensors, and ground-truth equipment deployed during the field campaign.

3.2. Equipment

3.2.1. Aerial Platforms and Sensors

During the campaign, two UAV platforms were deployed: a DJI Matrice 300 RTK (DJI, Shenzhen, China) equipped with a Zenmuse H20T camera (DJI, Shenzhen, China) and a DJI Matrice 30T (DJI, Shenzhen, China) featuring an integrated thermal imaging module. Both thermal sensors employ uncooled VOx microbolometer technology and operate within the 7.5 to 13.5 µm spectral range. They support two measurement modes: low gain (−40 °C to 550 °C) and high gain (−25 °C to 135 °C), with all acquisitions in this study performed in

low gain mode. Thermal images have a resolution of 640 × 512 pixels and a pixel pitch of 17 µm, according to the manufacturer's specifications [52,53].

The Zenmuse H20T camera is equipped with a 13.5 mm focal length lens that provides a field of view (FOV) of approximately 45° × 37°, while the DJI Matrice 30T uses a 9.1 mm focal length lens with an FOV of 47.7° × 37.0°. For both systems, the images were acquired at 0.5 frames per second. The DJI M300 platform was operated in both RTK-enabled and RTK-disabled modes to evaluate the effect of absolute positioning accuracy on geolocation performance, while the DJI M30T was used only in the RTK-disabled mode.

The onboard sensors provide the camera yaw, pitch, and roll angles directly in the NED world frame, facilitating the construction of the transformation matrix.

3.2.2. Image Exclusion Zone Parameters

As detailed in Section 2.2.4, an exclusion zone is defined in the image plane to mask pixels where the angle of incidence falls below the threshold $\delta_{\min} = 6°$, resulting in unreliable altitude estimates. This zone is modeled as an ellipse centered on the principal point of the image, with semiaxes a and b proportional to $\tan(\delta_{\min})$ and the intrinsic parameters of the sensor.

Based on sensor dimensions ($W = 7.68$ mm, $H = 6.144$ mm), image resolution (640 × 512 pixels), and focal lengths ($f = 13.5$ mm for the H20T and $f = 9.1$ mm for the M30T), the exclusion zones corresponding to $\delta_{\min} = 6°$ were calculated as elliptical masks of approximate pixel dimensions of 120 × 98 pixels for the H20T and 180 × 144 pixels for the M30T.

3.2.3. Hotspot Simulation and Ground Truth

Hotspots were generated using metal cans (diameter: 18 cm) filled with charcoal and ignition was performed using a dip torch (Figure 9).



Figure 9. Example of a simulated hotspot using a metal can filled with incandescent coal.

The ground truth coordinates of the simulated hotspot targets were recorded using a TERIA PYX RTK GNSS receiver (TERIA, Paris, France) [54], which provided centimeter-level accuracy under field conditions, with on-site precision better than 3 cm.

A total of 22 artificial hotspots were deployed during the field campaign: eight at the flat Porto-Vecchio site and 18 at the mountainous Soveria site.

At the Porto-Vecchio site, only four of the eight simulated hotspots remained incandescent and could be geolocated during the drone survey. The distances between these four detected targets ranged from approximately 20 m to 195 m.

At the Soveria site, the 18 simulated hotspots were strategically distributed to cover areas with local slopes ranging from a few degrees to 28° and with various slope orientations. The distances between the hotspots ranged from approximately 21 m to 348 m, and the elevation difference between the lowest and highest points of the site exceeds 100 m. Figure 10 shows the hotspot locations at the Soveria site, overlaid on Google Earth images.



Figure 10. Simulated hotspot locations (red) at the Soveria test site, displayed on Google Earth imagery.

At the flat Porto-Vecchio site, where the experiment was carried out in mid-November, the simulated hotspots clearly dominated the background, as the cool ambient conditions kept the soil and rock temperatures below 60 °C. Consequently, the detection threshold was set to 60 °C at this site. In contrast, at the mountainous Soveria site, where the experiment took place in late May, the ambient conditions were warmer, and the ground and rock surfaces locally reached 67 °C. To mitigate false detections from naturally heated surfaces, the detection threshold was increased to 100 °C at this site.

3.2.4. Digital Elevation Models

In this study, three DEMs were used. The primary dataset was the RGE ALTI® 1 m-resolution DEM [55], provided by the National Institute of Geographic and Forest Information (IGN) (Saint-Mandé, France) and covering the entire Corsican region. This national product is derived from a combination of airborne lidar surveys and photogrammetric stereo restitution from aerial imagery, depending on data availability across the territory. It consisted of 9281 tiles measuring 1 km × 1 km, each containing 1000 × 1000 elevation values, and was referenced in the Lambert 93 coordinate system. The complete data set required approximately 60 GB of disk storage and was used to quantitatively evaluate algorithm performance. To ensure consistency with the ground-truth data of the GNSS, the ellipsoidal heights (WGS84) measured by the RTK receiver were converted to orthometric heights using the EGM2008 geoid model. In Corsica, the RGE ALTI® DEM is referenced to the vertical datum IGN78C (NGF-IGN 1978 Corse [56]), while in mainland France the corresponding reference is IGN69 (NGF-IGN 1969 [57]).

To assess the sensitivity of the algorithm to spatial resolution, two coarser DEM were also considered for qualitative comparison: a 10 m version obtained by subsampling the 1 m dataset and a 25 m DEM provided in the BD ALTI product (IGN, Saint-Mandé, France) [58].

3.3. Flight Configurations

Flight missions were pre-programmed using the UgCS software (v5.10) [59] to maintain a constant height above ground level (AGL) with the terrain follow option activated. The UAV operated at a speed of 5 m/s, with a forward overlap of 75% and a side overlap of 50%.

At the Porto-Vecchio site, flights were conducted at 60 m AGL using both the DJI Matrice 300 (with H20T camera) and the DJI Matrice 30T, both without RTK positioning. At the Soveria site, flights were conducted at 60 m and 120 m AGL with terrain following enabled, using the DJI Matrice 300 with and without RTK, as well as the DJI Matrice 30T without RTK. These configurations were designed to evaluate the influence of flight height and absolute positioning accuracy on geolocation performance under contrasting topographic conditions.

3.4. Computation and Algorithm Deployment

Geolocation calculations and thermal image processing were performed on a dedicated computing platform, as described below. The algorithm requires DEM data to perform its computations.

The implementation was developed in Python version 3.10 and runs on a Dell Precision 3551 laptop with the following specifications: Intel Core i7-10850H CPU (2.70 GHz base, up to 5.10 GHz, 6 cores), 32 GB RAM, NVIDIA Quadro P620 GPU (4 GB VRAM), WDC SN730 NVMe SSD, and Windows 11 Professional 24H2 (64 bit).

The algorithm is deployed with a RESTful API, allowing flexible operation in both real-time and post-processing modes. In real-time mode, the live video stream is configured with a user-defined temperature range (default: 60–550 °C) and a predefined color palette. The isothermal thermal images are then extracted from the live stream and transmitted to the computer using the API for immediate analysis. In post-processing mode, the API handles radiometric thermal images in batch. During this process, the user is asked to specify a temperature threshold for hotspot segmentation (default: 60 °C).

4. Results

This section presents the results of the field experiments and the quantitative evaluation of the proposed hotspot geolocation method. The interpretation of these results is provided separately in Section 5. The performance of the method was evaluated at the two test sites described in Section 3.1. Quantitative geolocation accuracy was assessed using the 1 m-resolution DEM by comparing the estimated hotspot positions and cluster centroids derived from thermal images with the known ground-truth positions of the simulated hotspots. Additional tests were conducted to examine the influence of the spatial resolution of DEM (10 m and 25 m) and to compare the proposed method with a GNSS-based vertical projection baseline. Unless otherwise stated, cluster-level averages are unweighted.

4.1. Step-by-Step Example of DEM Traversal and Stopping Criterion

To illustrate the operation of the proposed method, the intermediate results for a representative hotspot are reported below. The example corresponds to a hotspot detected with a temperature threshold of 60 °C using a 1 m DEM. The centroid of the connected region in the image plane is located at the pixel coordinates $(u, v) = (33, 341)$ (Figure 11).

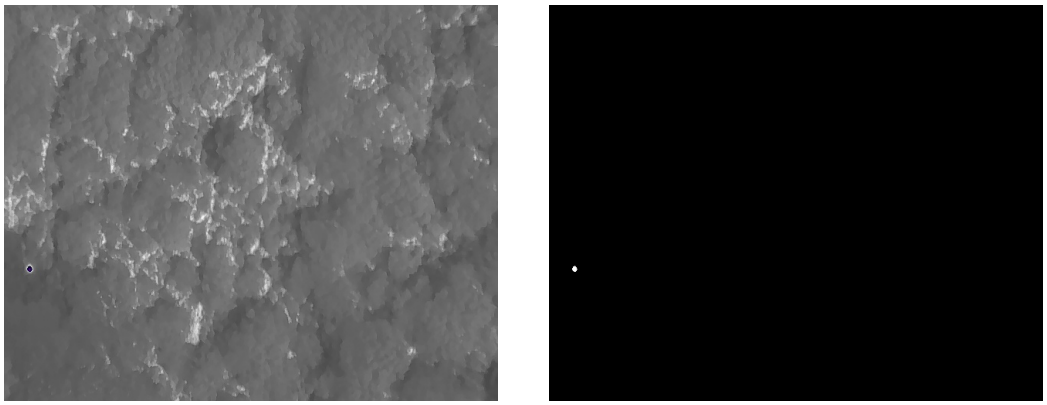

(**a**) (**b**)

Figure 11. Illustrative example of hotspot detection: (**a**) radiometric image with isothermal filter; (**b**) binary mask of the detected hotspot.

The initial configuration of this example is summarized in Table 1. It includes the position of the UAV, the DEM cell where the optical ray projection starts, the 2D direction vector (d_x, d_y) used in the traversal, and the incidence angle δ of the optical ray relative to the vertical.

Table 1. Setup of the parameters used for the step-by-step DEM traversal example.

Quantity	Value
Drone GNSS (lat, lon, alt)	42.3467572862583°N , 9.14679921234292°E, 824.842 m (WGS84)
Origin DEM cell (indices)	$(i_0, j_0) = (0, 0)$
Origin DEM cell (E_0, N_0) [m]	1,206,826.0, 6,158,264.0 (Lambert–93; bottom-left)
2D direction (d_x, d_y)	$(-0.255194636, -0.031260305)$
Incidence angle δ	14.898°

From this initialization, the DEM is traversed cell by cell in the local ENU frame introduced in Section 2.2. The DEM cell that contains the projection of the UAV optical center is taken as the origin $(i_0, j_0) = (0, 0)$, with Lambert–93 bottom-left coordinates (E_0, N_0) given in Table 1. For each visited cell (i, j), the elevation of the terrain z is compared to the estimated altitude of the optical ray z_r computed as described in Section 2.2. The traversal continues while $z_r > z$; the first cell where $z \geq z_r$ marks the ray–terrain intersection and defines the hotspot position.

As summarized in Table 2, the traversal stops at $k = 19$, corresponding to the DEM cell $(i, j) = (-19, -2)$ where the elevation of the terrain becomes greater than or equal to the altitude of the ray ($z \geq z_r$). Using the 1 m bottom-left convention, the Lambert–93 coordinates of the bottom-left corner of that cell are

$$(E, N) = (E_0 + i,\ N_0 + j) = (1,206,807.0,\ 6,158,262.0)$$

where E and N denote Easting and Northing, respectively. Applying the Lambert–93 inverse transformation yields the corresponding WGS84 geographic coordinates:

$$(\text{lat, lon}) = (42.34675729°\text{N},\ 9.146799212°\text{E})$$

Table 2. Step-by-step DEM traversal in the local ENU frame with the stopping criterion. All numerical values are rounded to the nearest tenth for readability.

k	(i, j)	z-Terrain (m)	z_r-Optical Ray (m)	$\Delta = z_r - z$ (m)	Decision
0	(0,0)	714.4	773.9	59.5	continue
1	(−1,0)	713.7	770.2	56.5	continue
2	(−2,0)	712.9	766.4	53.5	continue
3	(−3,0)	712.4	762.7	50.3	continue
4	(−4,0)	711.9	758.9	47.0	continue
5	(−5,−1)	711.4	754.8	43.4	continue
6	(−6,−1)	710.8	751.1	40.3	continue
7	(−7,−1)	710.2	747.4	37.2	continue
8	(−8,−1)	709.6	743.6	34.0	continue
9	(−9,−1)	708.9	739.9	31.0	continue
10	(−10,−1)	708.2	736.2	28.0	continue
11	(−11,−1)	707.6	732.4	24.8	continue
12	(−12,−1)	706.9	728.7	21.8	continue
13	(−13,−2)	706.3	724.5	18.2	continue
14	(−14,−2)	705.7	720.8	15.1	continue
15	(−15,−2)	705.1	717.0	11.9	continue
16	(−16,−2)	704.5	713.3	8.8	continue
17	(−17,−2)	704.0	709.6	5.6	continue
18	(−18,−2)	703.5	705.9	2.4	continue
19	(−19,−2)	702.8	702.1	−0.7	**stop**

GPS position (WGS84): 42.34675729°N, 9.146799212°E.

4.2. Geolocation Performance Metrics

Each simulated hotspot could be associated with one or more geolocated points detected in multiple thermal images acquired during the UAV flight (Figure 12). As the UAV moved along its trajectory, a given hotspot could appear in several thermal images, resulting in a set of geolocated points corresponding to the same ground-truth position. These points form a spatial cluster around the actual hotspot location, as described in the clustering step (Section 2.2.4).



Figure 12. Geolocated points (yellow) associated with simulated hotspots at the Soveria test site, overlaid on Google Earth imagery. Red markers indicate ground-truth hotspot positions.

Figure 13 shows the high-probability zones of hotspot presence, derived from the clusters of geolocated points presented in Figure 12. These zones were obtained by determining

the centroid and the maximum interpoint distance within each cluster. Each centroid was assigned a unique identifier to facilitate reference.



Figure 13. Centroids (shown in red and numbered) and contours (green) of the identified hotspot search zones at the Soveria test site, displayed on Google Earth imagery.

Six performance metrics were computed for each test configuration, capturing average and maximum errors at both point and centroid levels. For the first metric below, cluster-level means are weighted by cluster size.

- cluster-size weighted mean of per-cluster point positional errors (Weighted mean pt. error);
- average of per-cluster maximum point positional errors (Max pt. error);
- average centroid positional error (Centroid error);
- maximum of per-cluster mean point positional errors (Max of mean pt. error);
- maximum point positional error among all clusters (Max of max pt. error);
- maximum centroid positional error (Max centroid error).

The results of these metrics, calculated for all configurations tested with a 1 m-resolution DEM, are summarized in the Tables 3–5. In these tables, the abbreviations Mean pt., Max pt., and Centroid denote the average point positional error, maximum point positional error, and centroid positional error, respectively.

Table 3. Geolocation performance at the flat site (Porto-Vecchio), 60 m AGL, 1 m DEM.

UAV	Means [m]			Max [m]		
	Weighted Mean pt.	Max pt.	Centroid	Mean pt.	Max pt.	Centroid
M300 without RTK	3.6	4.4	3.4	4.2	4.7	4.0
M30T without RTK	3.4	3.9	3.0	4.3	4.9	3.8

Table 4. Geolocation performance at the mountainous site (Soveria), 60 m AGL, 1 m DEM.

UAV	Means [m]			Max [m]		
	Weighted Mean pt.	Max pt.	Centroid	Mean pt.	Max pt.	Centroid
M300 with RTK	3.1	5.0	2.5	4.1	7.8	3.7
M300 without RTK	3.3	5.1	2.5	4.3	7.0	3.9
M30T without RTK	4.7	7.4	4.2	5.7	9.7	5.4

Table 5. Geolocation performance at the mountainous site (Soveria), 120 m AGL, 1 m DEM.

UAV	Means [m]			Max [m]		
	Weighted Mean pt.	Max pt.	Centroid	Mean pt.	Max pt.	Centroid
M300 with RTK	3.5	6.0	2.4	5.3	12.6	4.5
M30T without RTK	4.8	7.0	3.5	7.0	11.0	6.6

4.3. Effect of DEM Resolution and Comparison with a GNSS Baseline

The DEM-based method was evaluated with 1, 10, and 25 m DEMs and compared to a GNSS vertical projection baseline under terrain-following flight conditions at 60 m and 120 m AGL. A total of 172 hotspots were analyzed at 60 m and 244 at 120 m. Table 6 reports the mean horizontal error, standard deviation, minimum and maximum errors, and the circular error probable at confidence levels of 50% and 95% (CEP50 and CEP95). All values are expressed in meters.

Table 6. Performance of the proposed method (three DEM resolutions) and the GNSS vertical projection baseline at two altitudes.

Height (m)	Method	Mean (m)	SD (m)	Min (m)	Max (m)	CEP95 (m)	CEP50 (m)
60	1 m DEM	3.15	1.77	0.91	11.86	6.06	2.92
	10 m DEM	7.86	3.71	3.13	20.03	14.43	7.10
	25 m DEM	17.80	7.57	2.27	37.01	31.24	16.01
	GNSS vertical projection	13.40	5.72	0.92	25.47	23.11	13.45
120	1 m DEM	4.12	2.51	1.04	14.04	10.39	3.77
	10 m DEM	8.70	3.86	3.13	21.99	15.68	8.07
	25 m DEM	17.30	8.12	2.27	46.45	30.47	14.81
	GNSS vertical projection	24.60	9.75	0.79	48.00	40.25	25.29

Figures 14 and 15 show the horizontal positional error distributions for the proposed method (DEMs of 1, 10, and 25 m) and for the GNSS vertical projection baseline at 60 m and 120 m AGL.

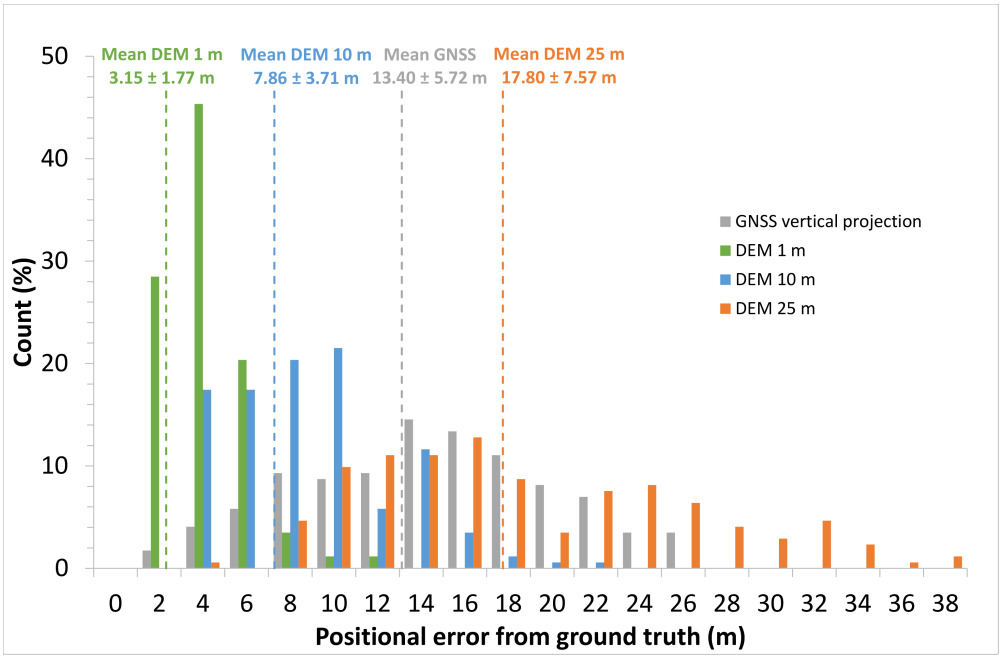

Figure 14. Error distribution at 60 m AGL for the proposed method (1, 10, 25 m DEMs) and the GNSS vertical projection baseline.

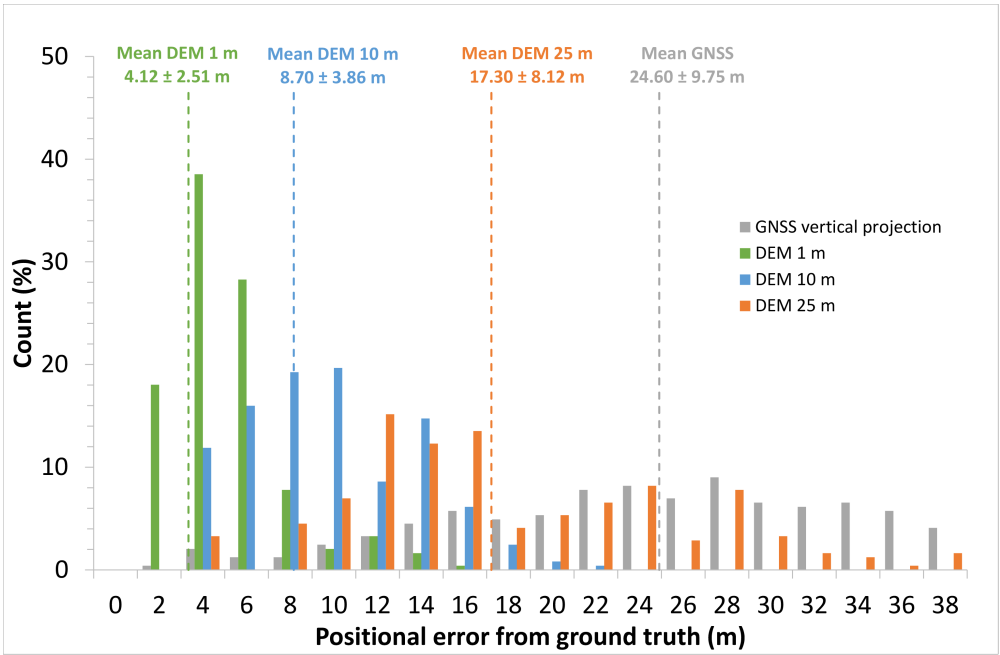

Figure 15. Error distribution at 120 m AGL for the proposed method (1, 10, 25 m DEMs) and the GNSS vertical projection baseline.

4.4. Processing Time

This subsection reports measured processing times under real-time and deferred (post-flight) execution. In both cases, the same geolocation pipeline is invoked; only the invocation pattern differs (frame-by-frame vs. batch).

Using the 1 m-resolution DEM, the full dataset of 847 radiometric thermal images acquired at 60 m AGL over the mountainous Soveria site was processed in 336 s (5 min 36 s), including hotspot detection and geolocation. This corresponds to an average of 0.40 s per image.

In real-time experiments with isothermal images, the RESTful API returned GPS coordinates of detected hotspots within the 2 s interval between successive image transmissions; no missed deadlines or observable queuing delays were recorded during these trials.

4.5. Operational Use in Real Wildfire Events

Independent of controlled field experiments, the deferred (post-flight) API implementing the proposed method with a 1 m DEM has been in routine operational use since July 2024 by the fire departments of South Corsica and North Corsica. In particular, it was used during the monitoring of a 38-hectare wildfire reactivation in Sotta (South Corsica) in 1 September 2024, when a complete batch of recorded thermal images was submitted to the API for hotspot geolocation. Figure 16 shows an aerial view of a portion of the monitored area during the intervention, while Figure 17 presents the locations of the detected hotspots.



Figure 16. Aerial view of part of the area covered by drone-based thermal imaging for hotspot geolocation during the Sotta wildfire on 1 September 2024. Photo courtesy of Jean-Baptiste Leca/SIS 2A.

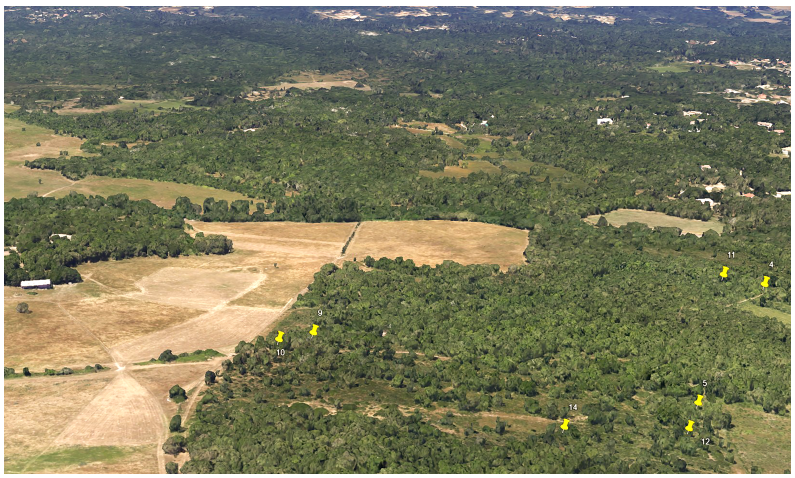

Figure 17. Google Earth visualization of geolocated hotspots for the 1 September 2024 Sotta wildfire.

5. Discussion

This section discusses the main factors that influence the geolocation performance of the proposed method and evaluates its robustness under different experimental conditions.

5.1. Geolocation Accuracy and Main Experimental Factors

The proposed method exhibits robust geolocation performance under the tested conditions, as centroid errors remained within a few meters across all configurations. The analysis further highlights that RTK positioning improves consistency in complex terrain, while increased flight altitude tends to enlarge the maximum point errors without significantly affecting centroid accuracy.

On the flat site (Porto-Vecchio, Table 3), both UAV platforms (M300 and M30T, without RTK) delivered similar performances, with Mean centroid errors of 3.4 m and 3.0 m, respectively, and Max centroid errors remaining below or equal to 4 m. The Mean pt. errors were approximately 3.5–3.6 m, while the Max pt. errors were 4.4 m and 3.9 m, respectively. These values reflect the spatial dispersion of the geolocated points within each cluster, with Max pt. errors reaching approximately 4–5 m. These results confirm that in flat terrain, with a DEM-resolution of 1 m, the method achieves Mean centroid errors of approximately

3 m and Max centroid errors below 4 m, even without RTK corrections, demonstrating its ability to deliver reliable geolocation estimates under favorable conditions.

On the mountain site at 60 m AGL (Table 4), the M300 with RTK showed the best performance, with a Mean centroid error of 2.5 m and a Max centroid error of 3.7 m. The same UAV without RTK achieved comparable Mean centroid errors (2.5 m) but with somewhat higher Max centroid errors. The M30T without RTK exhibited increased errors in this complex terrain, with a Mean centroid error of 4.2 m and a Max centroid error of 5.4 m, and a Max point error of 9.7 m. These results demonstrate that the method maintains Mean centroid errors below 4.5 m across all tested configurations, while the use of high-precision equipment further reduces errors when available.

At higher altitude (Soveria, 120 m AGL, Table 5), the M300 with RTK maintained a low Mean centroid error (2.4 m), demonstrating that even at 120 m AGL, the method delivers accurate geolocation estimates. However, the impact of increased flight altitude was evident in the Max point error, which increased to 12.6 m. In particular, the M30T without RTK achieved an improved Mean centroid error compared to 60 m AGL (3.5 m versus 4.2 m), while its Max centroid error remained limited to 6.6 m. Despite the expected increase in dispersion at this altitude, the clustering step effectively mitigated these effects, producing centroid estimates within acceptable error margins (typically below 5–6 m).

To further assess the influence of terrain and geometric factors, a quantitative analysis was performed to evaluate potential correlations between positioning error and parameters such as local slope angle, slope orientation, drone trajectory and delta angle. No significant relationships were observed, with the determination coefficients remaining below $R^2 < 0.16$ for all parameters tested, indicating that these factors did not have a measurable impact on the accuracy of the final location.

Overall, the method demonstrated consistent geolocation performance in all configurations, with RTK corrections and clustering contributing to improved accuracy and stability.

5.2. Effect of DEM Resolution on the Proposed Method and Comparison with the GNSS Vertical-Projection Baseline

The analysis highlights the influence of DEM resolution on the geolocation performance of the proposed method. As resolution decreases, the spatial dispersion of geolocated points tends to increase, resulting in slightly larger centroid uncertainties. In some cases, especially at 25 m resolution, nearby hotspots may no longer be clearly separated and can form merged clusters. Despite this expected degradation, the centroid positions remain broadly consistent with the locations of the simulated hotspots. This confirms that, while higher-resolution DEMs are preferable, the proposed method remains robust and usable even when only moderate- to low-resolution elevation data are available.

Compared with the GNSS vertical projection baseline, the DEM-based approach clearly outperforms the baseline at both altitudes and for all DEM resolutions, except for the 25 m DEM at 60 m AGL, where the baseline slightly outperforms the proposed method (13.40 m vs. 17.80 m mean error). At 120 m AGL, even with the 25 m DEM, the proposed method remains ahead (17.30 m vs. 24.60 m), indicating greater robustness as altitude increases.

5.3. Experimental Limitations and Environmental Constraints

One limitation concerns the test targets used in the experiments. The simulated hotspots, consisting of metal cans filled with incandescent wood and coal, provided a controlled and repeatable way to generate reference heat sources with known ground-truth positions. Although this experimental design does not reproduce the full diversity of residual hotspots, which can be more extended or cooler, part of the cans were deliberately placed under low vegetation to introduce partial occlusion. This choice aimed to

approximate more realistic field conditions beyond idealized targets while still ensuring reproducibility for quantitative assessment.

Another important aspect concerns the thermal detection threshold. In this study, thresholds were set to 60 °C at the Porto-Vecchio site (November) and 100 °C at the Soveria site (May), to avoid confusion with naturally heated surfaces. This does not represent a fixed constraint of the method, since the algorithm accepts user-defined thresholds that can be adapted to the operational context. Firefighters have highlighted this flexibility as particularly valuable, as it allows the detection sensitivity to be tuned in real time depending on the hour of operation, ambient heating, or the presence of smoke, thereby improving robustness under practical wildfire conditions.

For the flight configurations considered, it should be noted that the assumption of negligible residual lens distortions remains valid for the altitudes considered in this study (60–120 m AGL), where the method targets geolocation accuracies on the order of a few meters. This assumption was also verified to 30 m AGL, provided the same target accuracy is maintained. However, operations below 30 m AGL in vegetated environments were not considered, as canopy occlusion and geometric constraints would represent dominant limitations under such conditions.

Within the scope of environmental constraints, wind-related effects on measurement accuracy are largely mitigated by platform stabilization. The UAVs employed in this study are equipped with stabilized three-axis gimbals, which effectively compensate for short-term attitude perturbations due to wind or turbulence. As a result, the impact of adverse weather conditions on the orientation of the optical sensor is expected to be limited in the tested configurations. However, strong winds may still indirectly affect geolocation accuracy by reducing the overall positional stability of the platform, for example, through GNSS fluctuations or transient gimbal saturation. These conditions were avoided during field experiments, but they remain a potential source of error in operational deployments.

Another limitation concerns the effect of the vegetation canopy on the detectability of the hotspot. Dense or closed canopies can attenuate or completely block the thermal signal emitted by subsurface or ground-level hotspots, making them undetectable from aerial infrared imagery. This limitation is intrinsic to thermal remote sensing and restricts the applicability of the method in forested environments. In the present study, field experiments were carried out in Mediterranean maquis vegetation, where the canopy is discontinuous and the simulated hotspots remained visible from above.

5.4. Processing Efficiency and Operational Deployment

Using a 1 m DEM, the pipeline processes thermal images in 0.4 s per image on average, consistent with near-real-time throughput. Identical outputs were obtained in both real-time and deferred (post-flight) modes, confirming reproducibility across acquisition and processing workflows.

Since mid-2024, the deferred (post-flight) API has been operated by the fire departments of South and North Corsica. During post-containment monitoring of the 38-hectare wildfire in Sotta (South Corsica) on 1 September 2024, the API processed a complete batch of recorded thermal images and returned geolocated hotspot outputs, demonstrating field-scale applicability.

6. Conclusions

This paper presented a novel method for the geolocation of thermal hotspots, designed to operate on complex terrains. The experimental validation covered two representative sites, ranging from flat terrain to mountain maquis with slopes up to 28°, thus demonstrating the applicability of the approach in contrasting topographic conditions. Its originality

lies in traversing the digital elevation model (DEM) using a reformulated Bresenham combined with a lightweight, ray-tracing-inspired strategy for detecting the intersection of the optical ray with the terrain using an efficient cell-level altitude approximation.

A field experiment conducted over flat and mountainous terrains, with slopes of up to 28° and an elevation difference exceeding 100 m, using DJI Matrice 300 drones (with and without RTK) and Matrice 30T (without RTK), demonstrated that the method achieves robust and reliable geolocation. For images acquired at 60 m and 120 m above ground level, the method consistently achieved mean position errors below 4.2 m, confirming its effectiveness and geolocation accuracy under challenging conditions.

The key contribution of the study is the DEM-based geolocation principle, which determines the ground intersection of thermal optical rays through an efficient combination of grid traversal and altitude estimation. This approach, presented in Section 2.2, constitutes the main methodological advance of the article, distinguishing it from previous DEM-based strategies that were oversimplified or computationally demanding.

These results confirm the robustness and efficiency of the approach and highlight its potential integration into operational tools to support the planning of wildfire intervention in complex environments. Future work will focus on extending the method to accommodate arbitrary camera orientations and to support a wider range of airborne platforms beyond UAVs.

Author Contributions: Conceptualization, L.R., F.M., A.B., J.B., C.W., A.T. and A.P.; Formal analysis, A.B.; Funding acquisition, L.R.; Investigation, L.R., A.B., J.B., C.W., A.T. and A.P.; Methodology, L.R., A.B., C.W. and A.T.; Project administration, L.R.; Software, A.B., J.B., C.W. and A.T.; Supervision, L.R.; Validation, L.R., F.M., A.B., J.B., C.W., A.T. and A.P.; Visualization, F.M., A.B. and J.B.; Writing—original draft, L.R. and A.B.; Writing—review & editing, L.R., F.M. and A.B. All authors have read and agreed to the published version of the manuscript.

Funding: This research was funded by the Corsican Region and the French State in the framework of the collaborative project GOLIAT (CPER:40031) [60], with additional support from a maturation grant by SATT Sud-Est and internal funds of the University of Corsica.

Data Availability Statement: The raw data supporting the conclusions of this article will be made available by the authors on request.

Conflicts of Interest: The authors declare no conflict of interest.

References

1. United Nations Environment Programme (UNEP). Spreading Like Wildfire—The Rising Threat of Extraordinary Landscape Fires. A UNEP Rapid Response Assessment. *Nairobi*, 2022. Available online: https://www.unep.org/resources/report/spreading-wildfire-rising-threat-extraordinary-landscape-fires (accessed on 15 July 2025).
2. Duchelle, A. Increase in Climate-Driven Wildfires Calls for More Investment in Prevention. *UN Denmark*, 2024. Available online: https://un.dk/increase-in-climate-driven-wildfires-calls-for-more-investment-in-prevention/ (accessed on 15 July 2025).
3. European Science & Technology Advisory Group (E-STAG). *Evolving Risk of Wildfires in Europe: The Changing Nature of Wildfire Risk Calls for a Shift in Policy Focus from Suppression to Prevention*; United Nations Office for Disaster Risk Reduction (UNDRR): Brussels, Belgium, 2020.
4. Jones, M.W.; Abatzoglou, J.T.; Veraverbeke, S.; Andela, N.; Lasslop, G.; Forkel, M.; Smith, A.J.P.; Burton, C.; Betts, R.A.; van der Werf, G.R.; et al. Global and Regional Trends and Drivers of Fire Under Climate Change. *Rev. Geophys.* **2022**, *60*, e2020RG000726. [CrossRef]
5. Organisation for Economic Co-operation and Development (OECD). *Taming Wildfires in the Context of Climate Change*; OECD Publishing: Paris, France, 2023. [CrossRef]
6. Abatzoglou, J.T.; Pellegrini, A.; Maestre, F.T.; Seddon, A.W.R.; van der Werf, G.; Canadell, J.G. Climate change is increasing the risk of extraordinary landscape fires. *Nat. Ecol. Evol.* **2024**, *8*, 1420–1425. [CrossRef]
7. UK Government. *Heat Summary—Chapter 10: Wildfires and Health*; UK Health Security Agency: London, UK, 2022. Available online: https://www.gov.uk/guidance/heat-summary-chapter-10-wildfires-and-health (accessed on 15 July 2025).

8. Carrington, D. Summer Wildfires Increased Fourfold in England in 2022. *The Guardian*, 30 December 2022. Available online: https://www.theguardian.com/world/2022/dec/30/summer-wildfires-increased-fourfold-in-england-in-2022 (accessed on 15 July 2025).
9. International Association of Fire and Rescue Services (CTIF). The Biggest Fire in Slovenia's History: Karst Fire 2022. *CTIF*, 2023. Available online: https://ctif.org/sites/default/files/2023-06/CTIF%20The%20biggest%20fire.pdf (accessed on 15 July 2025).
10. European Commission. *Report on the Large Wildfires of 2022 in Europe*; Joint Research Centre: Brussels, Belgium, 2023. Available online: https://civil-protection-knowledge-network.europa.eu/system/files/2024-12/report-on-the-large-wildfires-of-2022-in-europe-kjna32034enn.pdf (accessed on 15 July 2025).
11. Reuters. Switzerland Fights to Contain Forest Fire near Italy Border as Winds Pick Up. *Reuters*, 2023. Available online: https://www.reuters.com/world/europe/swiss-forest-fire-could-spread-if-winds-pick-up-authorities-warn-2023-07-18/ (accessed on 15 July 2025).
12. Le News. Firefighters Continue to Fight Swiss Forest Fire. *LeNews*, 2023. Available online: https://lenews.ch/2023/07/22/firefighters-continue-to-fight-swiss-forest-fire/ (accessed on 15 July 2025).
13. Indian Express. *Drought, Rising Heat Bring Unusual Wildfire Warnings in Northern Europe*. 19 June 2023. Available online: https://indianexpress.com/article/world/drought-rising-heat-bring-unusual-wildfire-warnings-northern-europe-8667188/ (accessed on 15 July 2025).
14. Arctic Council. *Norwegian Chairship Launches Initiative to Address Wildland Fires*. 30 May 2023. Available online: https://arctic-council.org/news/norwegian-chairship-arctic-wildland-fires-initiative/ (accessed on 15 July 2025).
15. La Dépêche. Incendies en Gironde: Un an et demi après, pourquoi le feu couve-t-il toujours dans les sols ? *La Dépêche*, 2023. Available online: https://www.ladepeche.fr/2023/11/30/incendies-en-gironde-un-an-et-demi-apres-le-brasier-pourquoi-le-feu-couve-t-il-toujours-dans-les-sols-11612692.php (accessed on 15 July 2025).
16. Préfecture de la Gironde. Incendies en cours en Gironde—Point du 22 juillet 2022. *Gouvernement Français*, 2022. Available online: https://www.gironde.gouv.fr/Actualites/Communiques-de-presse/Communiques-de-presse-2022/Juillet-2022/Incendies-en-cours-en-Gironde-point-du-22-juillet-2022-a-20h00 (accessed on 15 July 2025).
17. Huijnen, V.; Wooster, M.J.; Kaiser, J.W.; Gaveau, D.L.A.; Flemming, J.; Parrington, M.; Inness, A.; Murdiyarso, D.; Main, B.; van Weele, M. Fire carbon emissions over maritime Southeast Asia in 2015 largest since 1997. *Sci. Rep.* **2016**, *6*, 26886. [CrossRef] [PubMed]
18. Turetsky, M.R.; Benscoter, B.; Page, S.; Rein, G.; van der Werf, G.R.; Watts, A. Global vulnerability of peatlands to fire and carbon loss. *Nat. Geosci.* **2015**, *8*, 11–14. [CrossRef]
19. Nolter, M.A.; Vice, D.H. Looking back at the Centralia coal fire: A synopsis of its present status. *Int. J. Coal Geol.* **2004**, *59*, 99–106. [CrossRef]
20. Stracher, G.B. Coal fires burning around the world: A global catastrophe. *Int. J. Coal Geol.* **2004**, *59*, 1–6. [CrossRef]
21. Incendies en Gironde: Des Drones Pour Repérer les Points Chauds Dans la Forêt de Cendre d'Hostens. Available online: https://www.youtube.com/watch?v=441e1KyNzYI (accessed on 15 July 2025).
22. Advexure. Firewatch from Above: How Thermal Drones Aid Wildfire Prevention and Response. *Advexure Blog*, 2025. Available online: https://advexure.com/blogs/news/firwatch-from-above-how-thermal-drones-aid-wildfire-prevention-response (accessed on 15 July 2025).
23. Fagen, C.; Weir, J.R.; Payne, D. Using Drones with Infrared Capabilities to Monitor Fire Behavior. Oklahoma Cooperative Extension Service. NREM-2907. 2021. Available online: https://extension.okstate.edu/fact-sheets/using-drones-with-infrared-capabilities-to-monitor-fire-behavior.html (accessed on 15 July 2025).
24. Iizuka, K.; Watanabe, K.; Kato, T.; Putri, N.A.; Silsigia, S.; Kameoka, T.; Kozan, O. Visualizing the Spatiotemporal Trends of Thermal Characteristics in a Peatland Plantation Forest in Indonesia: Pilot Test Using Unmanned Aerial Systems (UASs). *Remote Sens.* **2018**, *10*, 1345. [CrossRef]
25. He, X.; Yang, X.; Luo, Z.; Guan, T. Application of unmanned aerial vehicle (UAV) thermal infrared remote sensing to identify coal fires in the Huojitu coal mine in Shenmu city, China. *Sci. Rep.* **2020**, *10*, 13895. [CrossRef]
26. Yuan, C.; Youmin, Z.; Zhixiang, L. A survey on technologies for automatic forest fire monitoring, detection, and fighting using unmanned aerial vehicles and remote sensing techniques. *Can. J. For. Res.* **2015**, *45*, 783–792. [CrossRef]
27. Akhloufi, M.A.; Couturier, A.; Castro, N.A. Unmanned Aerial Vehicles for Wildland Fires: Sensing, Perception, Cooperation and Assistance. *Drones* **2021**, *5*, 15. [CrossRef]
28. Nex, F.; Remondino, F. Preface: Latest Developments, Methodologies, and Applications Based on UAV Platforms. *Drones* **2019**, *3*, 26. [CrossRef]
29. Bailon-Ruiz, R. Design of a Wildfire Monitoring System Using Fleets of Unmanned Aerial Vehicles. Ph.D. Thesis, Université Fédérale Toulouse Midi-Pyrénées, Toulouse, France, 24 September 2020. Available online: https://theses.hal.science/tel-02995471 (accessed on 28 November 2023).

30. Ambrosia, V.G.; Wegener, S.S.; Sullivan, D.V.; Buechel, S.W.; Dunagan, S.E.; Brass, J.A.; Stoneburner, J.; Schoenung, S.M. Demonstrating UAV Acquired Real Time Thermal Data over Fires. *Photogramm. Eng. Remote Sens.* **2003**, *69*, 246–253. [CrossRef]
31. Ollero, A.; de Dios, J.M.; Merino, L. Unmanned aerial vehicles as tools for forest-fire fighting. *For. Ecol. Manag.* **2006**, *234*, S263. [CrossRef]
32. Ambrosia, V.G.; Wegener, S.; Zajkowski, T.; Sullivan, D.V.; Buechel, S.; Enomoto, F.; Lobitz, B.; Johan, S.; Brass, J.; Hinkley, E. The Ikhana unmanned airborne system (UAS) western states fire imaging missions: From concept to reality (2006–2010). *Geocarto Int.* **2011**, *26*, 85–101. [CrossRef]
33. Hinkley, E.A.; Zajkowski, T. USDA forest service—NASA: Unmanned aerial systems demonstrations—Publishing the leading edge in fire mapping. *Geocarto Int.* **2011**, *26*, 103–111. [CrossRef]
34. Martins, A.; Almeida, J.; Almeida, C.; Figueiredo, A.; Santos, F.; Bento, D.; Silva, H.; Silva, E. Forest fire detection with a small fixed wing autonomous aerial vehicle. *IFAC Proc. Vol.* **2007**, *40*, 168–173. [CrossRef]
35. Merino, L.; Caballero, F.; Martínez-de Dios, J.R.; Ferruz, J.; Ollero, A. A cooperative perception system for multiple UAVs: Application to automatic detection of forest fire. *J. Field Robot.* **2006**, *23*, 165–184. [CrossRef]
36. Bailon-Ruiz, R.; Lacroix, S. Wildfire remote sensing with UAVs: A review from the autonomy point of view. In Proceedings of the 2020 International Conference on Unmanned Aircraft Systems (ICUAS), Athens, Greece, 1–4 September 2020. [CrossRef]
37. Saffre, F.; Hildmann, H.; Karvonen, H.; Lind, T. Monitoring and Cordoning Wildfires with an Autonomous Swarm of Unmanned Aerial Vehicles. *Drones* **2022**, *6*, 301. [CrossRef]
38. Pastor, E.; Barrado, C.; Royo, P.; Santamaria, E.; Lopez, J.; Salami, E. Architecture for a helicopter-based unmanned aerial systems wildfire surveillance system. *Geocarto Int.* **2011**, *26*, 113–131. [CrossRef]
39. Keerthinathan, P.; Amarasingam, N.; Hamilton, G.; Gonzalez, F. Exploring unmanned aerial systems operations in wildfire management: Data types, processing algorithms and navigation. *Int. J. Remote Sens.* **2023**, *44*, 5628–5685. [CrossRef]
40. Wright, D.B.; Yotsumata, T.; El-Sheimy, N. Real time identification and location of forest fire hotspots from geo-referenced thermal images. *Int. Arch. Photogramm. Remote Sens. Spat. Inf. Sci.* **2004**, *35*, 13–18.
41. Graml, R.; Grant, W. Bushfire Hotspot Detection Through Uninhabited Aerial Vehicles and Reconfigurable Computing. In Proceedings of the IEEE Aerospace Conference, Big Sky, MT, USA, 1–8 March 2008; pp. 1–13. [CrossRef]
42. Allison, R.; Johnston, J.M.; Craig, G.; Jennings, S. Airborne Optical and Thermal Remote Sensing for Wildfire Detection and Monitoring. *Sensors* **2016**, *16*, 1310. [CrossRef]
43. Viseras, A.; Marchal, J.; Schaab, M.; Pages, J.; Estivill, L. Wildfire Monitoring and Hotspots Detection with Aerial Robots: Measurement Campaign and First Results. In Proceedings of the 2019 IEEE International Symposium on Safety, Security, and Rescue Robotics (SSRR), Würzburg, Germany, 2–4 September 2019. [CrossRef]
44. Lin, Z.; Bohdanov, D.; Liu, H.H.T.; Wotton, M. Autonomous wildfire hotspot detection using a fixed wing UAV. *Int. J. Aerosp. Syst. Sci. Eng.* **2021**, *1*, 68–84. [CrossRef]
45. Cai, Y.; Zhou, Y.; Zhang, H.; Xia, Y.; Qiao, P.; Zhao, J. Review of Target Geo-Location Algorithms for Aerial Remote Sensing Cameras without Control Points. *Appl. Sci.* **2022**, *12*, 12689. [CrossRef]
46. Whitted, T. An improved model for shaded display. *Comun. ACM* **1980**, *23*, 343–349. [CrossRef]
47. Bresenham, J.C. Algorithm for Computer Control of a Digital Plotter. *IBM Syst. J.* **1965**, *4*, 25–30. [CrossRef]
48. Malgouyres, R. *Algorithmes pour la Synthèse D'images et L'animation 3D*; Dunod: Paris, France, 2005; pp. 11–19.
49. Collins, R.T.; Tsin, Y.; Miller, J.R.; Lipton, A.J. Using a DEM to determine Geospatial Object Trajectories. In *DARPA Image Understanding Workshop*; Morgan Kaufmann Publishers: San Francisco, CA, USA, 1998; Volume 1.
50. Santana, B.; Cherif, E.K.; Bernardino, A.; Ribeiro, R. Real-Time Georeferencing of Fire Front Aerial Images Using Iterative Ray-Tracing and the Bearings-Range Extended Kalman Filter. *Sensors* **2022**, *22*, 1150. [CrossRef] [PubMed]
51. El Arfaoui, W. *Wildfire Mapping Using Infra-Red Images Acquired by a Drone*; Trainee Report; INP-ENSEEIHT: Toulouse, France, 2019.
52. DJI. *Zenmuse H20 Series v1.2*; SZ DJI Technology Co., Ltd.: Shenzhen, China, 2021. Available online: https://dl.djicdn.com/downloads/Zenmuse_H20_Series/20200824/Zenmuse_H20_Series_User_Manual-EN.pdf (accessed on 15 July 2025).
53. DJI. Matrice 30 Series User Manual v2.2. 2024. Available online: https://dl.djicdn.com/downloads/matrice-30-series/20230922UM/Matrice30_Series_User_Manual_v2.0_EN.pdf (accessed on 15 July 2025).
54. TERIA. Fiche Technique Récepteur GNSS PYX. 2022. Available online: https://www.reseau-teria.com/wp-content/uploads/fiche-technique-pyx.pdf (accessed on 15 July 2025).
55. Institut National de l'information Géographique et Forestière (IGN). RGE ALTI®—Référentiel à Grande Échelle Altimétrique. Available online: https://geoservices.ign.fr/rgealti (accessed on 15 July 2025).
56. *NGF-IGN 1978*; Nivellement Général de la France—Réseau de Corse. IGN: Saint-Mandé, France, 1978.
57. *NGF-IGN 1969*; Nivellement Général de la France—Réseau de Base. IGN: Saint-Mandé, France, 1969.
58. Institut National de l'information Géographique et Forestière (IGN). BD ALTI®—Base de Données Altimétrique. Available online: https://geoservices.ign.fr/bdalti (accessed on 15 July 2025).

59. SPH Engineering. Flight Planning Software for UAV Missions. Available online: https://www.sphengineering.com/flight-planning (accessed on 15 July 2025).
60. The GOLIAT Project. Available online: https://goliat.universita.corsica/?lang=en (accessed on 15 July 2025).

Disclaimer/Publisher's Note: The statements, opinions and data contained in all publications are solely those of the individual author(s) and contributor(s) and not of MDPI and/or the editor(s). MDPI and/or the editor(s) disclaim responsibility for any injury to people or property resulting from any ideas, methods, instructions or products referred to in the content.